

# Thesis Title

by

E. Ross



A thesis submitted to the  
University of Birmingham  
for the degree of  
DOCTOR OF PHILOSOPHY

Solar and Stellar Physics Group (SASP)  
School of Physics and Astronomy  
University of Birmingham  
Birmingham, B15 2TT  
Month 20XX

# Abstract

You're awesome. Make sure the examiners know it

# Acknowledgements

Who do you hate least?

# Contents

|  |             |
|--|-------------|
| <b>Abstract</b>  | <b>i</b>    |
| <b>Acknowledgments</b>   | <b>ii</b>   |
| <b>List of Figures</b>   | <b>vii</b>  |
| <b>List of Tables</b>  | <b>viii</b> |
| <b>List of Abbreviations</b>   | <b>ix</b>   |
| <b>1 HiSPARC as a Space Weather Detector</b>                                 | <b>1</b>    |
| 1.1 Introduction . . . . .   | 1           |
| 1.1.1 HiSPARC Project . . . . .  | 1           |
| 1.1.2 HiSPARC Detector . . . . .   | 2           |
| 1.2 Aims . . . . .   | 4           |
| 1.3 HiSPARC Properties . . . . .   | 4           |
| 1.4 HiSPARC Observations . . . . .   | 8           |
| 1.4.1 HiSPARC Observations of Ground Level Enhancements . . . . .            | 9           |
| 1.4.2 HiSPARC Observations of Forbush Decreases . . . . .                    | 9           |
| 1.5 Air Shower Simulations . . . . .   | 10          |
| 1.5.1 Air Shower Footprints . . . . .  | 13          |
| 1.5.2 Muon Flux . . . . .  | 15          |
| 1.6 Standardisation of HiSPARC Data . . . . .                                | 15          |
| 1.6.1 Motivation . . . . .   | 15          |
| 1.6.2 Barometric Correction . . . . .  | 17          |
| 1.6.3 Temperature Correction . . . . .                                       | 19          |
| 1.7 HiSPARC Observations After Pressure Corrections . . . . .                | 22          |
| 1.7.1 Pressure Corrected Observations of Ground Level Enhancements . . . . . | 22          |
| 1.7.2 Pressure Corrected Observations of Forbush Decreases . . . . .         | 23          |
| 1.8 Discussion . . . . .   | 23          |
| 1.9 Conclusion . . . . .   | 23          |
| <b>2 HiSPARC Station 14008</b>   | <b>25</b>   |
| 2.1 Introduction . . . . .   | 25          |
| 2.2 Aims . . . . .   | 26          |
| 2.3 HiSPARC 14008 Detector Set-up . . . . .                                  | 26          |
| 2.3.1 Configuration . . . . .  | 26          |

|       |                                  |           |
|-------|----------------------------------|-----------|
| 2.3.2 | Calibration . . . . .            | 27        |
| 2.3.3 | Monitoring Temperature . . . . . | 28        |
| 2.4   | Observations . . . . .           | 29        |
| 2.5   | Conclusions . . . . .            | 29        |
|       | <b>Bibliography</b>              | <b>29</b> |

# List of Figures

|     |   |    |
|-----|---|----|
| 1.1 | Schematic diagram of the HiSPARC scintillation detector. (A): PMT;<br>(B): light-guide adaptor; (C): light-guide; (D): scintillator. . . . .  | 3  |
| 1.2 | Typical formations of 2-detector and 4-detector stations. In each, the grey circle denotes a GPS antenna which is located in between the detectors to provide a precise timestamp for each signal. . . . .  | 5  |
| 1.3 | Azimuthal and zenith angle variations in the allowed and forbidden rigidity trajectories for HiSPARC station 501. . . . .   | 7  |
| 1.4 | The vertical asymptotic viewing directions of 5 HiSPARC stations. The rigidity range of the simulations were from $1.0 \text{ GV} < R < 20.0 \text{ GV}$ , and the results are plotted in geographic coordinates on January 20th 2005. The diamonds correspond to the HS ground location and the circles correspond to the AVD for a specific rigidity value. . . . .       | 8  |
| 1.5 | HiSPARC data for stations 501 and 3001 around the epoch of GLE 70. The plot shows the minute-averaged and 5-minute-averaged trigger events between detectors within the station. The vertical red, dashed line depicts the approximate onset time of the GLE. . . . .   | 9  |
| 1.6 | HiSPARC data for stations 8001 and 3001 around the epoch of GLE 71. The plot shows the minute-averaged and 5-minute-averaged trigger events between detectors within the station. The vertical red, dashed line depicts the approximate onset time of the GLE. . . . .  | 10 |
| 1.7 | HiSPARC data for 4 stations around the epoch of GLE 72. The top panel of each subplot shows the minute-averaged trigger events between detectors within the station, while the bottom panel shows the mean-shifted, minute-averaged counts by each individual detector in the station. The vertical red, dashed line depicts the approximate onset time of the GLE. . . . . | 11 |
| 1.8 | HiSPARC data for stations 501 and 8001 around the epoch of the FDs in March 2012. The plot shows the minute-averaged and hourly-averaged trigger events between detectors within the station. The vertical blue-dashed lines show the approximate onset-time of the FDs. . . . .  | 13 |
| 1.9 | HiSPARC data for stations 501 and 8001 around the epoch of the FD in July 2012. The plot shows the minute-averaged and hourly-averaged trigger events between detectors within the station. The vertical blue-dashed line shows the approximate onset-time of the FD. . . . .   | 13 |

|      |  |    |
|------|--|----|
| 1.10 | HiSPARC data for 4 stations around the epoch of the FD in December 2014. The plot shows the minute-averaged and hourly-averaged trigger events between detectors within the station. The vertical blue-dashed line shows the approximate onset-time of the FD. . . . .   | 14 |
| 1.11 | HiSPARC data for [n] stations around the epoch in which there were several FDs close to the onset of GLE 72. The top panel of each subplot shows the minute-averaged trigger events between detectors within the station, while the bottom panel shows the mean-shifted, minute-averaged counts by each individual detector in the station. The vertical blue-dashed lines show the approximate onset-times of the two FDs observed around this epoch and the red-dashed line depicts the approximate onset time of the GLE. . . . . | 15 |
| 1.12 | Mean muon density footprints for (a) proton-initiated air showers and (b) $\alpha$ -particle-initiated air showers with intial PCR trajectories with zenith angles $\theta = 0^\circ$ and various PCR energies. The error bars given represent $1\sigma$ . . . . .   | 16 |
| 1.13 | Mean number of muons produced at ground level by the PCR for (a) proton-initiated air showers and (b) $\alpha$ -particle-initiated air showers, for various PCR energy. The uncertainty bars given represent $1\sigma$ . . . . .   | 16 |
| 1.14 | .....  | 17 |
| 1.15 | The barometric coefficient calculation: (a) during November 2017 for the South Pole (SOPO) NM station, (b) during November 2019 for HiSPARC station 501 at Nikhef. . . . .   | 18 |
| 1.16 | A comparison between the monthly barometric coefficient computed in this work and using the online barometric coefficient tool throughout the year 2017 for the SOPO NM station. . . . .   | 19 |
| 1.17 | Pressure corrected HiSPARC data for 2 stations around the epoch of GLE 71. The top panel of each subplot shows the minute-averaged trigger events between detectors within the station, while the bottom panel shows the mean-shifted, minute-averaged counts by each individual detector in the station. The vertical red, dashed line depicts the approximate onset time of the GLE. . . . .   | 22 |
| 1.18 | Pressure corrected HiSPARC data for 2 stations around the epoch of GLE 72. The top panel of each subplot shows the minute-averaged trigger events between detectors within the station, while the bottom panel shows the mean-shifted, minute-averaged counts by each individual detector in the station. The vertical red, dashed line depicts the approximate onset time of the GLE. . . . .   | 22 |
| 1.19 | .....  | 23 |
| 1.20 | .....  | 23 |

|      |   |    |
|------|---|----|
| 1.21 | Pressure corrected HiSPARC data for [n] stations around the epoch in which there were several FDs close to the onset of GLE 72. The top panel of each subplot shows the minute-averaged trigger events between detectors within the station, while the bottom panel shows the mean-shifted, minute-averaged counts by each individual detector in the station. The vertical blue-dashed lines show the approximate onset-times of the two FDs observed around this epoch and the red-dashed line depicts the approximate onset time of the GLE. . . . . | 24 |
| 2.1  | Schematic diagram of the HiSPARC station 14008 detector set-up. . . . .   | 26 |
| 2.2  | HiSPARC 14008 assembly and configuration. (a) shows the stacked arrangement of the scintillators on the lab work bench, between layers of protective foam. (b) shows the complete detector inside the ski-box on the University of Birmingham campus. . . . .   | 27 |
| 2.3  | Voltage calibration curve for the PMTs of station 14008. The upper, red-dashed line indicates the upper limit for the low threshold singles rate (400 Hz), and the lower 2, black-dashed lines indicate the upper and lower bounds for the high threshold singles rate (100–130 Hz). . . . .  | 28 |
| 2.4  | Schematic diagram of the DS18B20 temperature sensor circuit, whereby the voltage, ground, and GPIO interfaces connect directly into pins of the Raspberry Pi board. . . . .   | 29 |

# List of Tables

|     |   |    |
|-----|---|----|
| 1.1 | Properties of some of the HiSPARC stations: geographic longitude ( $\lambda$ ), geographic latitude ( $\phi$ ), altitude ( $h$ ), and the geomagnetic vertical cut-off rigidity ( $R_C$ ) calculated from the PLANETOCOSMICS simulations. . . . .             | 7  |
| 1.2 | Space weather events investigated within the HiSPARC data. The percentage change column provides a reference of how much the CR counts observed by the NM station at Oulu ( $R_c=0.81$ GV) increased or decreased by, due to the space weather event. . . . . | 9  |
| 1.3 | PCRs simulated using CORSIKA. . . . .   | 12 |

# List of Abbreviations

**AVD** Asymptotic Viewing Direction.

**CR** Cosmic Ray.

**EAS** Extensive Air Shower.

**FD** Forbush Decrease.

**GLE** Ground Level Enhancement.

**IGRF** International Geomagnetic Reference Field.

**MD** Muon Detector.

**NM** Neutron Monitor.

**PCR** Primary Cosmic Ray.

**PMMA** Polymethylmethacrylate.

**PMT** Photo Multiplier Tube.

**SCR** Solar Cosmics Ray.

**UHECR** Ultra-High Energy Cosmic Ray.

# 1 HiSPARC as a Space Weather Detector

## 1.1 Introduction

... [on daily variations (DV)] Dr. Rolf Butikofer (in a reply from Danislav Sapundzjiev, dasapund@meteo.be) said:

*"The daily cosmic ray variation near Earth is caused by the anisotropy of the cosmic ray intensity in the interplanetary space. Cosmic ray particles follow the field lines of the interplanetary magnetic field when they travel towards the interior of the heliosphere. Because of the rotation of the Earth, the angle between the asymptotic cone of acceptance of various energies at the location of ground-based cosmic ray detectors (neutron monitors) and the direction of the interplanetary magnetic field varies with a time period of 24 hours. As a consequence cosmic ray detectors look in different directions in the course of a day and observe therefore a diurnal variation. The daily variations of neutron monitors is mainly seen by high latitude stations which have asymptotic directions at low energies (rigidities) near the equator."*

### 1.1.1 HiSPARC Project

HiSPARC stands for ***H*igh *S*chool *P*roject on *A*strophysics and *R*esearch with *C*osmics**, and it is a scientific outreach project that was initiated in the Netherlands in 2002 (Bartels, 2012). The HiSPARC project has two main goals: the study of Ultra-High Energy Cosmic Ray (UHECR) for astroparticle physics research, and to serve as a resource to expose high school students to scientific research (Bartels, 2012).

HiSPARC is a global network of muon detectors spread across the Netherlands,

Denmark, the UK, and Namibia. The detectors at each station record muon counts and may be used for many scientific experiments, such as: reconstruction of the direction of a cosmic ray induced air shower, reconstruction of the energy of the air shower's primary particle, investigation between the atmospheric conditions and the number of cosmics rays observed, etc.

Data recorded by the HiSPARC stations are stored and are available publicly at <http://www.hisparc.nl>, where the Cosmic Ray (CR) counts, atmospheric data, station metadata, and more can be found.

### 1.1.2 HiSPARC Detector

- design
  - scintillators
  - typical layouts (i.e. 2d or 4d)
  - trigger conditions

The detection philosophy of HiSPARC is to sample the footprints of Extensive Air Shower (EAS) using scintillation detectors. As HiSPARC was set up as an outreach programme for high schools, this impacted detector design. Resources are limited in schools and the detectors are usually financed by the participating high schools, colleges, and universities. In addition, students (accompanied by their teachers and local node support staff) are responsible for assembly and installation their detectors, which are typically installed on the roofs of schools. Due to this, the detectors needed to be cheap, robust, and easily maintainable, therefore the scintillation detector was selected for the HiSPARC network.

Scintillators consist of materials that emit light when charged particles pass through them. The total light produced is proportional to the number of charged particles, and can be collected by a Photo Multiplier Tube (PMT). Each HiSPARC detector utilises a plastic scintillator of dimensions 1000 mm x 500 mm x 20 mm, providing a detection area of 0.5 m<sup>2</sup>. The scintillator is glued to a triangular/‘fish-

tailed' light-guide (dimensions, base:500 mm; top:25 mm; height:675 mm), and a light-guide adapter provides the optical interface between the square end of the light-guide and the cylindrical aperture of the PMT. The configuration of a single HiSPARC detector is shown in Figure 1.1.

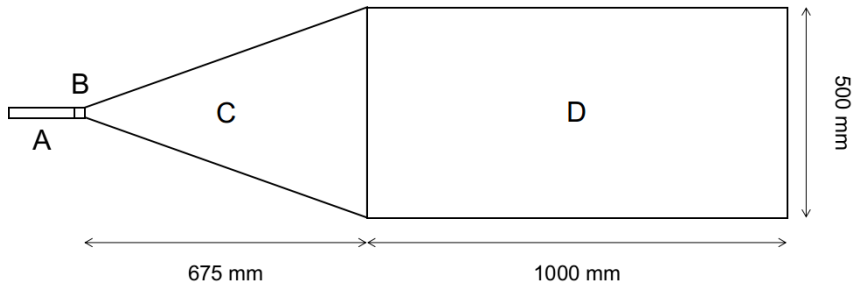


Figure 1.1: Schematic diagram of the HiSPARC scintillation detector. (A): PMT; (B): light-guide adaptor; (C): light-guide; (D): scintillator.

The scintillator is made of a material consisting of polyvinyltoluene as the base, with anthracene as the fluor, and the emission spectrum peaks at a wavelength of 425 nm (Fokkema, 2012; Bartels, 2012). The light-guide is made from Polymethylmethacrylate (PMMA) and has a comparable refractive index to the scintillator (1.58 and 1.49, respectively), reducing refraction effects between the two materials (van Dam et al., 2020).

The PMT used is an ETEEnterprises 9125B PMT, with a 25 mm aperture, blue-green sensitive bialkali photocathode, and 11 high-gain dynodes (?). The quantum efficiency of the PMT used in the HiSPARC detectors peaks at around 375 nm at 28%, and at 425 nm the quantum efficiency is 25% (Fokkema, 2012).

Each detector is wrapped in aluminium foil (thickness  $30 \mu\text{m}$ ) and a black, vinyl material (thickness 0.45 mm), which is usually used as a pond liner, to ensure light-tight detectors and to reduce the noise level from stray photons (van Dam et al., 2020). In addition, each detector is placed inside of its own a plastic ski-box to again ensure that it is light-tight, and to also ensure that it is weather-proof, as the detectors are usually located on the roofs of schools, colleges, and universities.

... from Vam Damm....: ...A vertically incident minimum ionizing particle has a

most probable energy loss in 2 cm scintillation material of 3.51 MeV ( 1 MIP)...

A HiSPARC station combines either 2 or 4 detectors, and typical configurations of each are shown in Figure 1.2. The separation between detectors varies from station-to-station. In addition some stations have the capability to measure the local atmospheric properties, such as temperature, pressure, relative humidity etc.

## 1.2 Aims

The HiSPARC project was set up with the detection philosophy of observing EAS, which are typically associated with Primary Cosmic Ray (PCR)s with energy of  $\sim 10^{14}$  eV and above, that produce large footprints observable with many HiSPARC stations simultaneously. For PCRs with energy below  $\sim 10^{14}$  eV the air shower is small, with almost no observable footprint, and for PCRs with energy below  $\sim 10^{11}$  eV, there are typically less than one or two muons that reach the ground, making their observation difficult.

The HiSPARC detectors are capable of observing any muons that reach them, therefore the project was motivated by the existing network of Muon Detector (MD) which may have the capability of observing the CRs associated with space weather events.

The principle aim of the project was to determine whether the existing HiSPARC network is capable of observing space weather events. This was initially achieved by investigating the data during periods of space weather activity to search for the associated signatures. In addition, simulations of air showers initiated by CRs were conducted to understand the expected muon flux at ground level.

## 1.3 HiSPARC Properties

- Selected HS stations - Locations of stations - PLANETOCOSMICS simulations (explain) - Rigidities - Asymptotic viewing directions

To understand the PCR spectrum that the HiSPARC stations are capable of



(a) 2-detector station configuration



(b) 4-detector station configuration (triangle arrangement)



(c) 4-detector station configuration (diamond arrangement)

Figure 1.2: Typical formations of 2-detector and 4-detector stations. In each, the grey circle denotes a GPS antenna which is located in between the detectors to provide a precise timestamp for each signal.

observing, PCR transport simulations were performed using the PLANETOCOSMICS software. PLANETOCOSMICS performs Geant4 Monte Carlo simulations of charged particle transport through Earth's magnetosphere based on Størmers transport equation for charged particles (Desorgher et al., 2006). PLANETOCOSMICS

simulates backward trajectories of charged particles from a given location (latitude, longitude, and altitude) out to the magnetopause for a set of PCR rigidities.

For each trajectory there are two possible outcomes: (i) the particles trace out to the magnetopause where they escape Earth's magnetosphere, an allowed trajectory; (ii) the particles are sufficiently bent by the effect of the Earth's magnetosphere that they do not reach the magnetopause and cannot escape the Earth's magnetosphere, a forbidden trajectory (Desorgher et al., 2006). The coordinates of the asymptotic direction at the magnetosphere are provided as an output to the simulations projected back down to the Earth's surface. In this work PLANETOCOSMICS was configured with the Tsyganenko-89 model for the external magnetospheric magnetic field and the International Geomagnetic Reference Field (IGRF) internal field model.

For each rigidity simulated, whether it was an allowed or forbidden trajectory was stored, which was used to provide an insight into the rigidity spectrum for a given station. From the allowed trajectories the effective cut-off rigidity ( $R_C$ ) for the stations was computed using equation (1.1), where  $R_U$  is the upper rigidity (the last allowed trajectory before the first forbidden trajectory);  $R_L$  is the lower rigidity (the last allowed trajectory before which all other trajectories with a lower rigidity are forbidden);  $\Delta R$  is the rigidity step size in the simulation (Desorgher et al., 2006; Herbst et al., 2013).

$$R_C = R_U - \sum_{i=R_L}^{R_U} \Delta R_i \quad (1.1)$$

The rigidity spectrum for each of the HiSPARC stations were investigated to determine  $R_C$  for each station. The cut-off rigidity calculated for the six HiSPARC stations for a vertical incidence upon the atmosphere (i.e.  $0^\circ$  zenith angle) are shown in Table 1.1 which show that there is little variation in  $R_C$  between the HiSPARC stations and that they observe protons with rigidities in excess of  $\sim 3$  GV. This analysis was initially carried out for the vertical direction (i.e. azimuth =

Table 1.1: Properties of some of the HiSPARC stations: geographic longitude ( $\lambda$ ), geographic latitude ( $\phi$ ), altitude ( $h$ ), and the geomagnetic vertical cut-off rigidity ( $R_C$ ) calculated from the PLANETOCOSMICS simulations.

| Station Name/ID             | $R_C$<br>[GV] | $\lambda$<br>[deg] | $\phi$<br>[deg] | $h$<br>[m] | No. Detectors |
|-----------------------------|---------------|--------------------|-----------------|------------|---------------|
| Nikhef/501                  | 3.19          | 4.95 E             | 52.36 N         | 56.18      | 4             |
| College Hageveld/203        | 3.18          | 4.63 E             | 52.35 N         | 53.71      | 2             |
| Leiden/3001                 | 3.23          | 4.45 E             | 52.17 N         | 54.08      | 2             |
| Eindhoven/8001              | 3.44          | 5.49 E             | 51.45 N         | 70.12      | 2             |
| Birmingham University/14001 | 3.06          | 1.93 W             | 52.45 N         | 204.14     | 4             |

$0^\circ$ , zenith =  $0^\circ$ ); however further trajectories were simulated for different azimuth and zenith angles to determine the dependence of the rigidity spectrum on the detector acceptance angle. The analysis for the azimuthal dependence was carried out at a zenith angle of  $20^\circ$  as this is around the most probable angle for HiSPARC events, and the analysis of the zenith dependence was carried out at an azimuth angle of  $0^\circ$ .

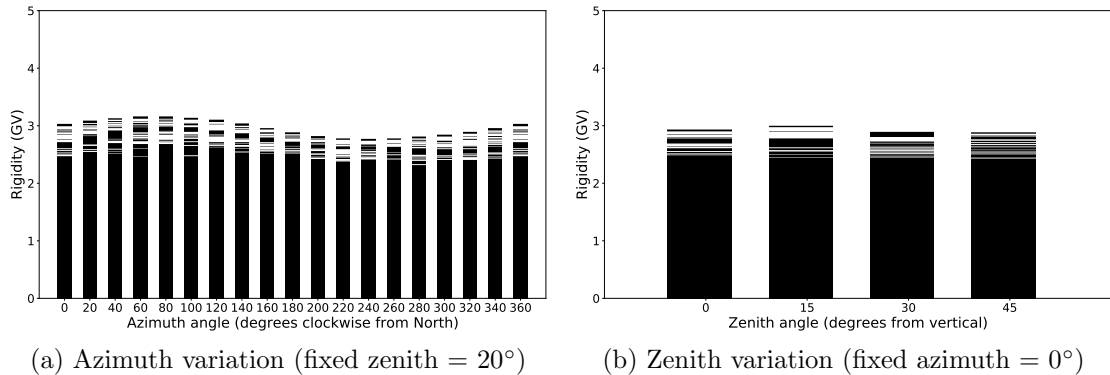


Figure 1.3: Azimuthal and zenith angle variations in the allowed and forbidden rigidity trajectories for HiSPARC station 501.

The small variation between HiSPARC stations is due to their close proximity in geographic latitude and longitude. The values of  $R_C$  calculated for the HiSPARC stations suggest that they should be able to observe higher energy Solar Cosmics Ray (SCR), but may not be as susceptible as the higher latitude Neutron Monitor (NM) where the effects of Ground Level Enhancement (GLE)s are highly observable.

As a result of the PLANETOCOSMICS simulations it is possible to understand

the trajectories of particles that enter the Earth's magnetosphere prior to arrival at the muon detector.

Figre 1.4... Asymptotic Viewing Direction (AVD)...

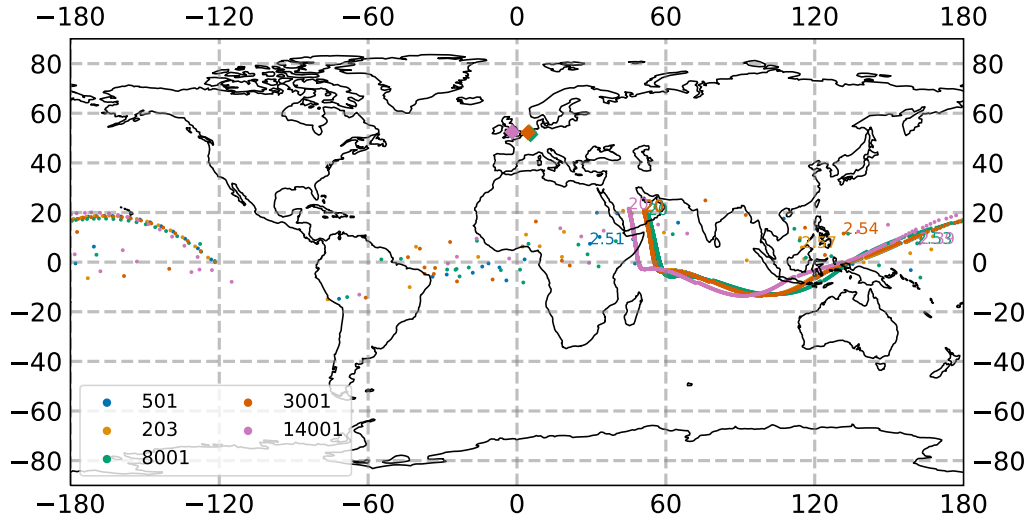


Figure 1.4: The vertical asymptotic viewing directions of 5 HiSPARC stations. The rigidity range of the simulations were from  $1.0 \text{ GV} < R < 20.0 \text{ GV}$ , and the results are plotted in geographic coordinates on January 20th 2005. The diamonds correspond to the HS ground location and the circles correspond to the AVD for a specific rigidity value.

## 1.4 HiSPARC Observations

[discuss preliminary observation of space weather Forbush Decrease (FD)s and GLEs for the events and singles data...]

[end with discussion on unknown PCRs observable and the effect of atmospheric weather conditions that need to be accounted for]

The effects of space weather on CR has been outlined in [REF intro]. It was highlighted during private communication with the UK Met Office that observations of GLEs are of more interest and importance to space weather forecasts and nowcasts. FD are of lower interest and importance, however they were still searched for within the HiSPARC data. The events that were looked for within the HiSPARC data are outlined in Table 1.2.

Table 1.2: Space weather events investigated within the HiSPARC data. The percentage change column provides a reference of how much the CR counts observed by the NM station at Oulu ( $R_c=0.81$  GV) increased or decreased by, due to the space weather event.

| GLE Onset  | GLE | % Change (Oulu) | FD Onset   | % Change (Oulu) |
|------------|-----|-----------------|------------|-----------------|
| 13/12/2006 | 70  | ~ 100%          | 08/03/2012 | ~ 10%           |
| 17/05/2012 | 71  | ~ 15%           | 12/03/2012 | ~ 3 – 5%        |
| 10/09/2017 | 72  | ~ 5%            | 14/07/2012 | ~ 3%            |
|            |     |                 | 21/12/2014 | ~ 5%            |
|            |     |                 | 06/09/2017 | ~ 2%            |
|            |     |                 | 07/09/2017 | ~ 8%            |

#### 1.4.1 HiSPARC Observations of Ground Level Enhancements

Initial searches for evidence of GLEs within the HiSPARC data were conducted for GLE 70, 71, and 72, as they are the only GLEs that span the operational epoch of the HiSPARC network.

Figure 1.5...

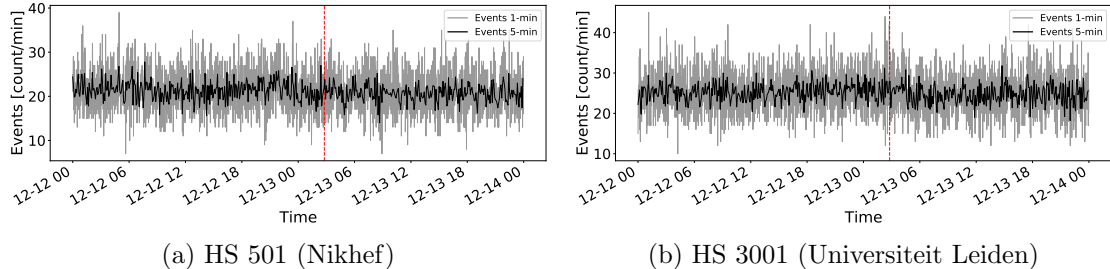


Figure 1.5: HiSPARC data for stations 501 and 3001 around the epoch of GLE 70. The plot shows the minute-averaged and 5-minute-averaged trigger events between detectors within the station. The vertical red, dashed line depicts the approximate onset time of the GLE.

Figure 1.6...

Figure 1.7...

... no clear GLEs seen...

#### 1.4.2 HiSPARC Observations of Forbush Decreases

From Lingri et al. (2016): "The majority of FDs are produced by CMEs with velocities from 400 to 1200 km/sec and at the same time the velocity of the solar wind

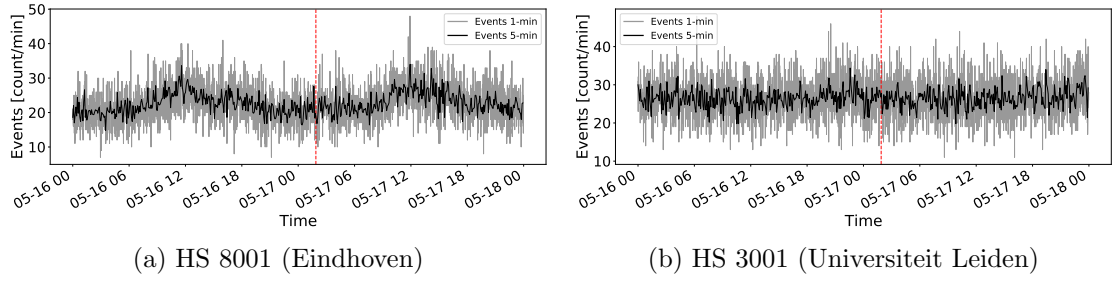


Figure 1.6: HiSPARC data for stations 8001 and 3001 around the epoch of GLE 71. The plot shows the minute-averaged and 5-minute-averaged trigger events between detectors within the station. The vertical red, dashed line depicts the approximate onset time of the GLE.

fluctuates from 400 to 740 km/sec”

Figure 1.8...

Figure 1.9...

Figure 1.10...

Figure 1.11...

... no clear FDs seen...

## 1.5 Air Shower Simulations

In order to understand the footprint of air showers produced by PCRs, simulations of air showers were performed for a range of primary proton and  $\alpha$ -particle energies.

To simulate the CR air shower development, we employ CORSIKA (**C**Osmic **R**ay **S**Imulations for **K**Ascade), a Monte Carlo programme providing detailed simulations of the evolution of air showers initiated by cosmic rays particles through the atmosphere (Heck & Pierog, 2017). The particles in the CORSIKA simulations are tracked through the atmosphere until they undergo interactions with atmospheric nuclei, decay due to their instability, or reach the ground level defined as the end of the simulation.

Proton and  $\alpha$ -particle initiated air showers were generated with energies ranging from  $10^9$  to  $10^{20}$  eV, and  $4 \times 10^9$  to  $10^{20}$  eV, respectively. In total  $\sim 230000$  proton-initiated showers were simulated and  $\sim 180000$   $\alpha$ -particle-initiated air show-

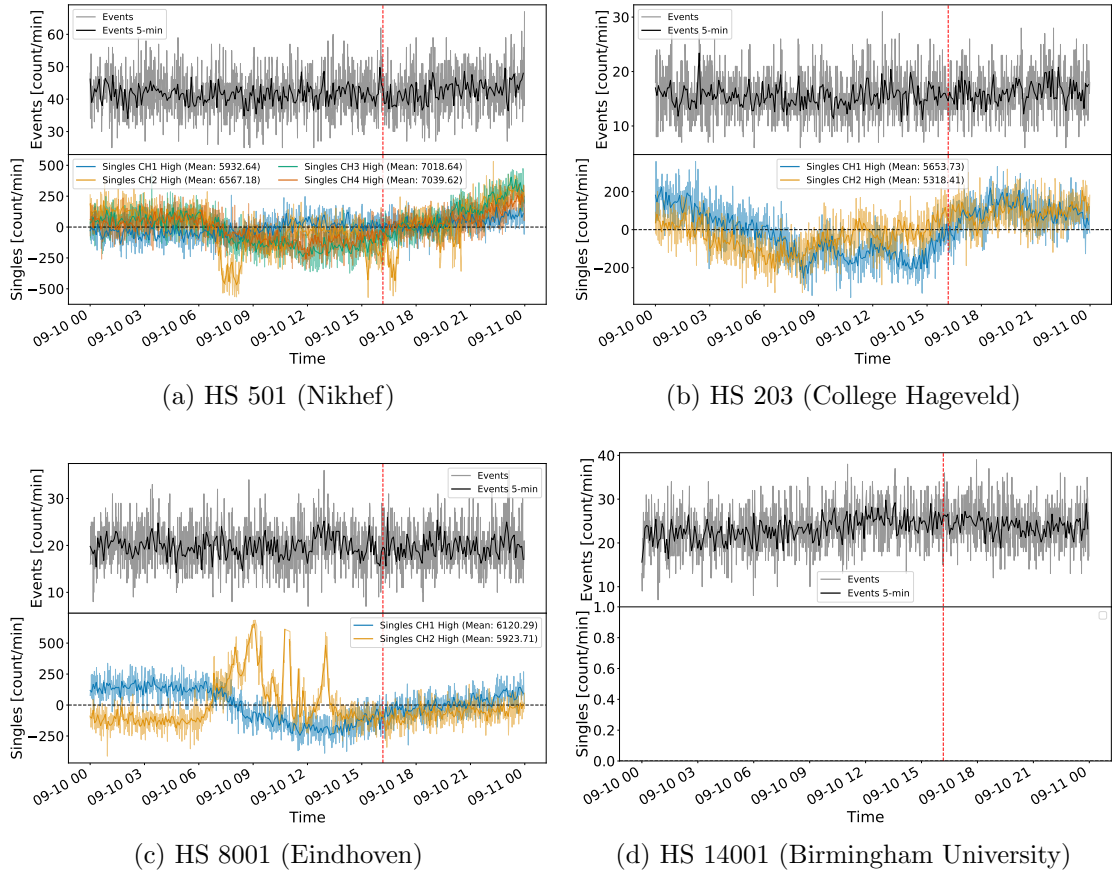


Figure 1.7: HiSPARC data for 4 stations around the epoch of GLE 72. The top panel of each subplot shows the minute-averaged trigger events between detectors within the station, while the bottom panel shows the mean-shifted, minute-averaged counts by each individual detector in the station. The vertical red, dashed line depicts the approximate onset time of the GLE.

ers were simulated. The list of simulated air shower PCRs is shown in Table 1.3. For high energy, inelastic hadronic interactions within CORSIKA the QGSJET-II [REF] model was selected. Interactions of hadrons with energies below 80 GeV are simulated using GHEISHA [REF], which allowed for the simulation of PCRs in the regime of SCRs. In addition to these hadronic interactions, electromagnetic interactions within the CORSIKA simulations were described by the EGS4 [REF] model. Furthermore CORSIKA has a minimum muon energy limit that can be simulated of 10 MeV.

There are several other user-definable setting within CORSIKA which are explained in-depth in the CORSIKA user's guide (Heck & Pierog, 2017). The settings

Table 1.3: PCRs simulated using CORSIKA.

| Protons               |                   |                       |                   | $\alpha$ -Particles   |                   |                       |                   |
|-----------------------|-------------------|-----------------------|-------------------|-----------------------|-------------------|-----------------------|-------------------|
| E <sub>PCR</sub> (eV) | N <sub>sims</sub> |
| 1.00E+09              | 10000             | 2.98E+12              | 1000              | 4.00E+09              | 10000             | 1.00E+13              | 1000              |
| 1.27E+09              | 10000             | 3.79E+12              | 1000              | 4.28E+09              | 10000             | 1.78E+13              | 100               |
| 1.62E+09              | 10000             | 4.83E+12              | 1000              | 5.46E+09              | 10000             | 3.16E+13              | 100               |
| 2.07E+09              | 10000             | 6.16E+12              | 1000              | 6.95E+09              | 10000             | 5.62E+13              | 100               |
| 2.64E+09              | 10000             | 7.85E+12              | 1000              | 8.86E+09              | 10000             | 1.00E+14              | 100               |
| 3.36E+09              | 10000             | 1.00E+13              | 1000              | 1.00E+10              | 10000             | 1.78E+14              | 50                |
| 4.28E+09              | 10000             | 1.78E+13              | 100               | 1.13E+10              | 10000             | 3.16E+14              | 50                |
| 5.46E+09              | 10000             | 3.16E+13              | 100               | 1.44E+10              | 10000             | 5.62E+14              | 50                |
| 6.95E+09              | 10000             | 5.62E+13              | 100               | 1.83E+10              | 10000             | 1.00E+15              | 10                |
| 8.86E+09              | 10000             | 1.00E+14              | 100               | 2.34E+10              | 10000             | 1.78E+15              | 10                |
| 1.00E+10              | 10000             | 1.78E+14              | 50                | 2.98E+10              | 10000             | 3.16E+15              | 10                |
| 1.13E+10              | 10000             | 3.16E+14              | 50                | 3.79E+10              | 10000             | 5.62E+15              | 10                |
| 1.44E+10              | 10000             | 5.62E+14              | 50                | 4.83E+10              | 10000             | 1.00E+16              | 10                |
| 1.83E+10              | 10000             | 1.00E+15              | 10                | 6.16E+10              | 10000             | 1.78E+16              | 10                |
| 2.34E+10              | 10000             | 1.78E+15              | 10                | 7.85E+10              | 10000             | 3.16E+16              | 10                |
| 2.98E+10              | 10000             | 3.16E+15              | 10                | 1.00E+11              | 10000             | 5.62E+16              | 10                |
| 3.79E+10              | 10000             | 5.62E+15              | 10                | 1.27E+11              | 1000              | 1.00E+17              | 10                |
| 4.83E+10              | 10000             | 1.00E+16              | 10                | 1.62E+11              | 1000              | 1.78E+17              | 10                |
| 6.16E+10              | 10000             | 1.78E+16              | 10                | 2.07E+11              | 1000              | 3.16E+17              | 10                |
| 7.85E+10              | 10000             | 3.16E+16              | 10                | 2.64E+11              | 1000              | 5.62E+17              | 10                |
| 1.00E+11              | 10000             | 5.62E+16              | 10                | 3.36E+11              | 1000              | 1.00E+18              | 10                |
| 1.27E+11              | 1000              | 1.00E+17              | 10                | 4.28E+11              | 1000              | 1.78E+18              | 10                |
| 1.62E+11              | 1000              | 1.78E+17              | 10                | 5.46E+11              | 1000              | 3.16E+18              | 10                |
| 2.07E+11              | 1000              | 3.16E+17              | 10                | 6.95E+11              | 1000              | 5.62E+18              | 10                |
| 2.64E+11              | 1000              | 5.62E+17              | 10                | 8.86E+11              | 1000              | 1.00E+19              | 10                |
| 3.36E+11              | 1000              | 1.00E+18              | 10                | 1.13E+12              | 1000              | 1.78E+19              | 10                |
| 4.28E+11              | 1000              | 1.78E+18              | 10                | 1.44E+12              | 1000              | 3.16E+19              | 10                |
| 5.46E+11              | 1000              | 3.16E+18              | 10                | 1.83E+12              | 1000              | 5.62E+19              | 10                |
| 6.95E+11              | 1000              | 5.62E+18              | 10                | 2.34E+12              | 1000              | 1.00E+20              | 10                |
| 8.86E+11              | 1000              | 1.00E+19              | 10                | 2.98E+12              | 1000              |                       |                   |
| 1.13E+12              | 1000              | 1.78E+19              | 10                | 3.79E+12              | 1000              |                       |                   |
| 1.44E+12              | 1000              | 3.16E+19              | 10                | 4.83E+12              | 1000              |                       |                   |
| 1.83E+12              | 1000              | 5.62E+19              | 10                | 6.16E+12              | 1000              |                       |                   |
| 2.34E+12              | 1000              | 1.00E+20              | 10                | 7.85E+12              | 1000              |                       |                   |

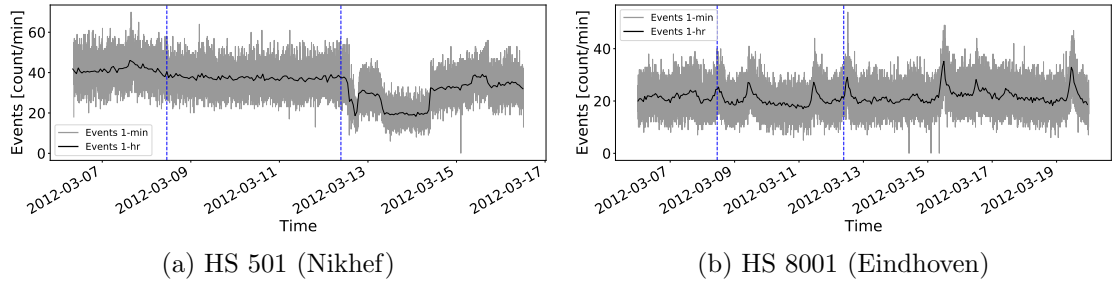


Figure 1.8: HiSPARC data for stations 501 and 8001 around the epoch of the FDs in March 2012. The plot shows the minute-averaged and hourly-averaged trigger events between detectors within the station. The vertical blue-dashed lines show the approximate onset-time of the FDs.

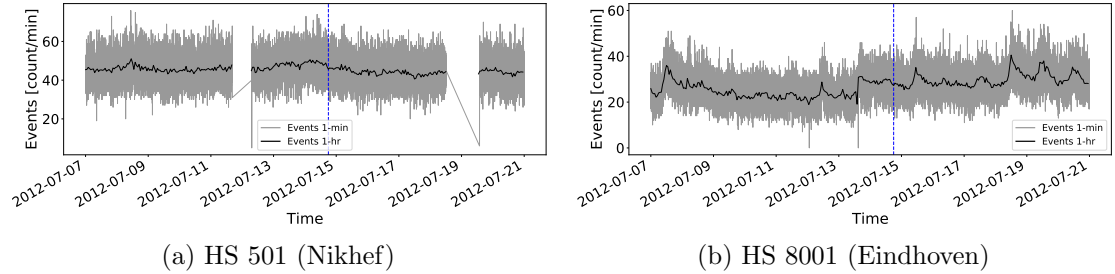


Figure 1.9: HiSPARC data for stations 501 and 8001 around the epoch of the FD in July 2012. The plot shows the minute-averaged and hourly-averaged trigger events between detectors within the station. The vertical blue-dashed line shows the approximate onset-time of the FD.

chosen within these simulation are briefly discussed below. Simulation thinning was enable in CORSIKA to reduce computation time and reduce the output file size. The observation level at which point the simulation cease was set at 100 m above sea level (compared to the  $\sim 50$  m typical of the stations, however this difference is negligible for the air shower development.) The pre-defined central European atmosphere in October was used for all simulations, and western-European magnetic field was used as calculated with the *Geomag* programme [REF]:  $B_x = 18.799 \mu\text{T}$  and  $B_z = 44.980 \mu\text{T}$ .

### 1.5.1 Air Shower Footprints

The average footprint of muons at ground level was acquired from the output CORSIKA simulations. This was achieved by simply taking the distributino of the muons

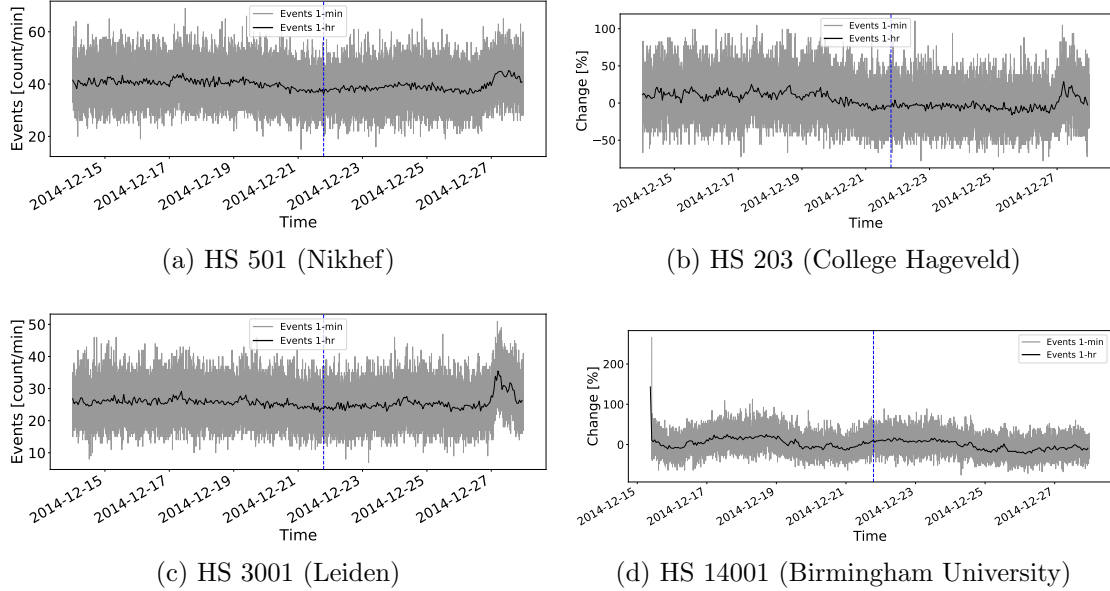


Figure 1.10: HiSPARC data for 4 stations around the epoch of the FD in December 2014. The plot shows the minute-averaged and hourly-averaged trigger events between detectors within the station. The vertical blue-dashed line shows the approximate onset-time of the FD.

at ground level at the end of the simulation as a function of their distance from the shower core for each individual simulation realisation. For a given PCR energy the average air shower footprint distribution is calculated by combining the individual simulation realisations.

The interpretation of Figure 1.12 can provide an understanding of the minimum energy of PCRs observable by the different stations within the HiSPARC network. The typical separation between the detectors in a HiSPARC station is  $\sim 10$  m, however the separation between detectors can be up to as much as 20 m or as low as a couple of metres. This analysis of the air shower footprint shows the variation in PCR energy sampled varies marginally over this range of distances and suggests that HiSPARC stations will typically observe PCR with an energy of  $\sim 10^{14} - 10^{15}$  eV to meet the required trigger conditions.

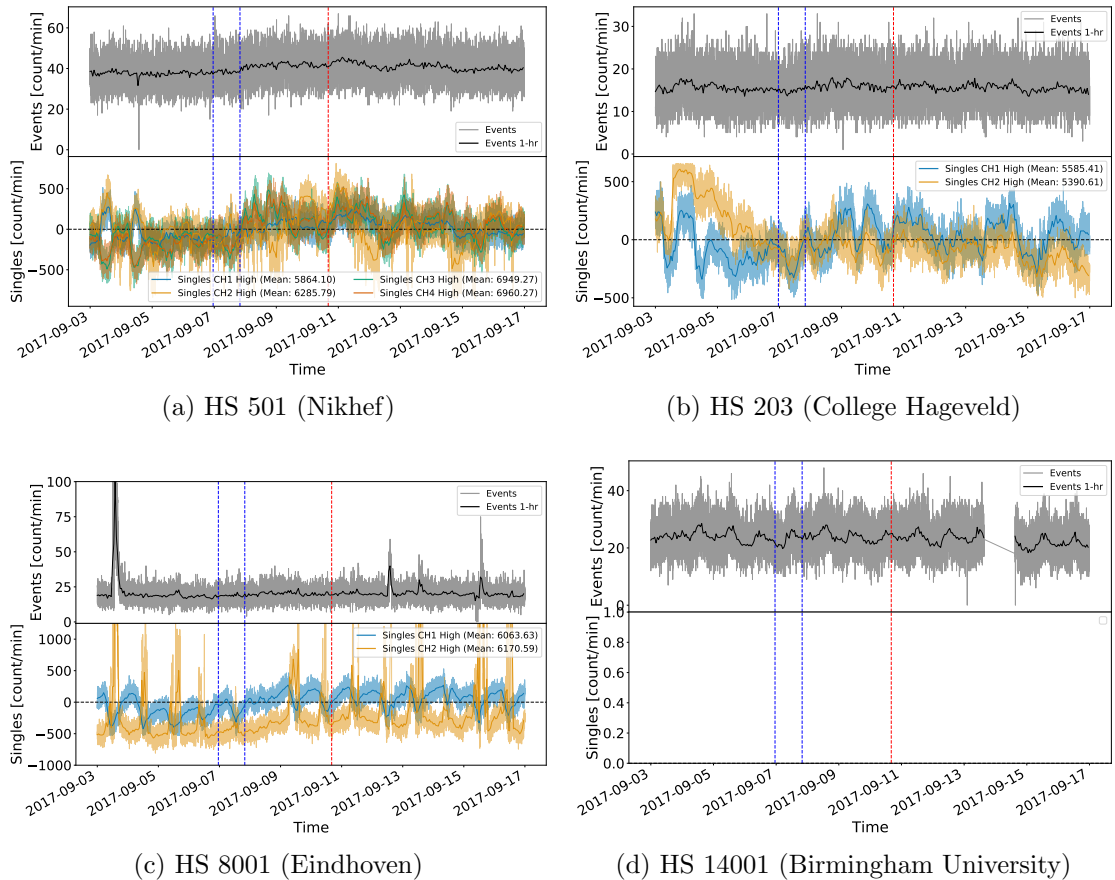


Figure 1.11: HiSPARC data for [n] stations around the epoch in which there were several FDs close to the onset of GLE 72. The top panel of each subplot shows the minute-averaged trigger events between detectors within the station, while the bottom panel shows the mean-shifted, minute-averaged counts by each individual detector in the station. The vertical blue-dashed lines show the approximate onset-times of the two FDs observed around this epoch and the red-dashed line depicts the approximate onset time of the GLE.

### 1.5.2 Muon Flux

From the air shower simulations it is possible to gain an estimate of the muon flux at ground-level based on the number of

## 1.6 Standardisation of HiSPARC Data

### 1.6.1 Motivation

- HiSPARC stations are individually managed and guidelines aren't stringent - Variability between stations exists and also apparently between detectors within a station

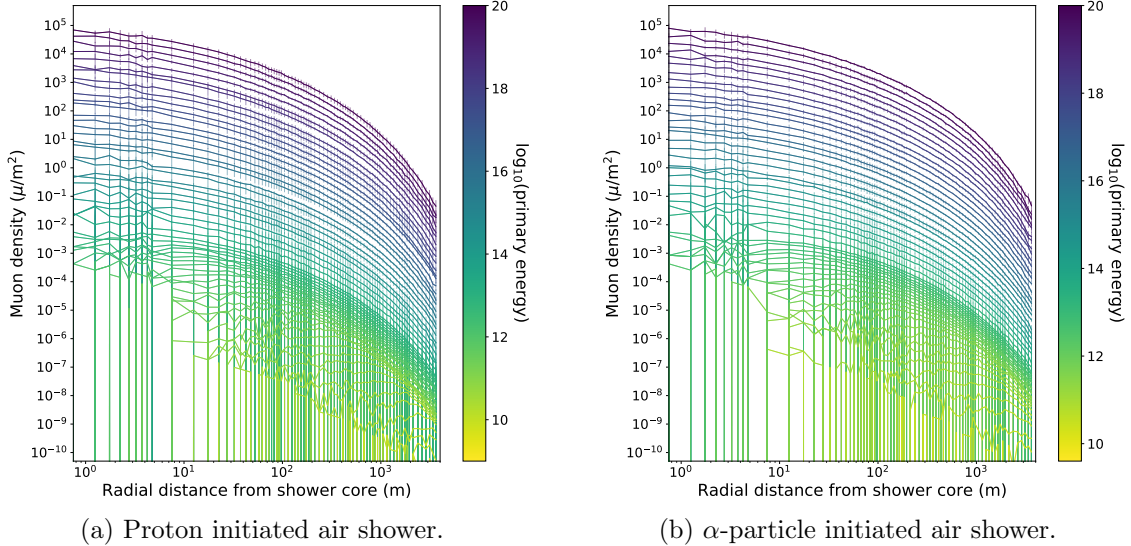


Figure 1.12: Mean muon density footprints for (a) proton-initiated air showers and (b)  $\alpha$ -particle-initiated air showers with initial PCR trajectories with zenith angles  $\theta = 0^\circ$  and various PCR energies. The error bars given represent  $1\sigma$ .

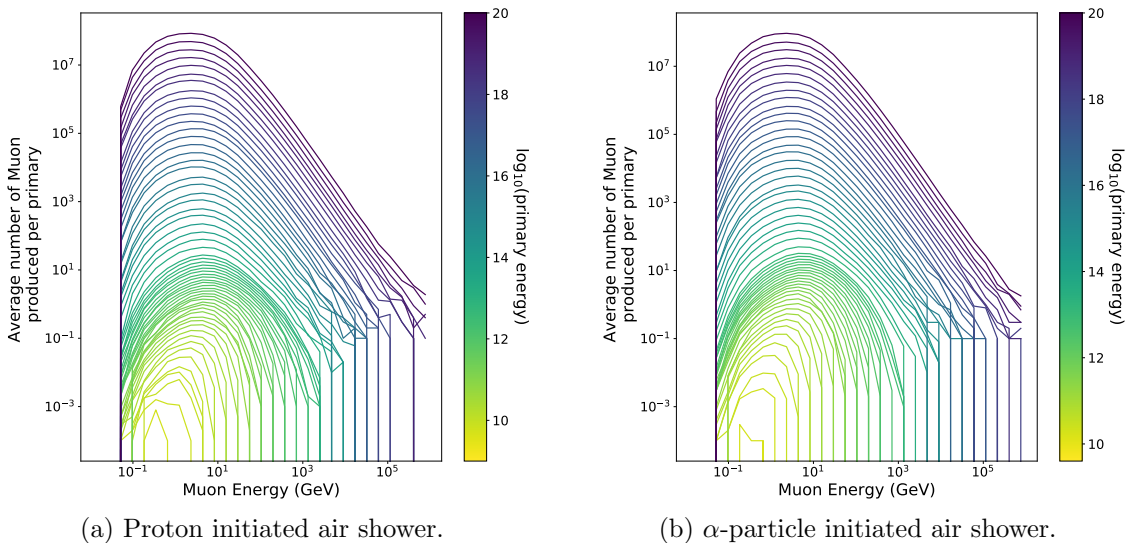


Figure 1.13: Mean number of muons produced at ground level by the PCR for (a) proton-initiated air showers and (b)  $\alpha$ -particle-initiated air showers, for various PCR energy. The uncertainty bars given represent  $1\sigma$ .

(i.e. see singles during GLE 72)

### 1.6.2 Barometric Correction

It is understood that observations made by ground-based CR detectors are susceptible to atmospheric conditions. Atmospheric pressure effects the CR travel path due to the expansion and contraction of the atmosphere with varying pressure; hence the CR counts are observed to be negatively correlated to atmospheric pressure as shown for both NMs and MDs in Figure 1.14. A correction for this barometric effect is routinely applied as part of the data calibration for all NM stations within the NMDB NEST, but there is no such process in the HiSPARC network.

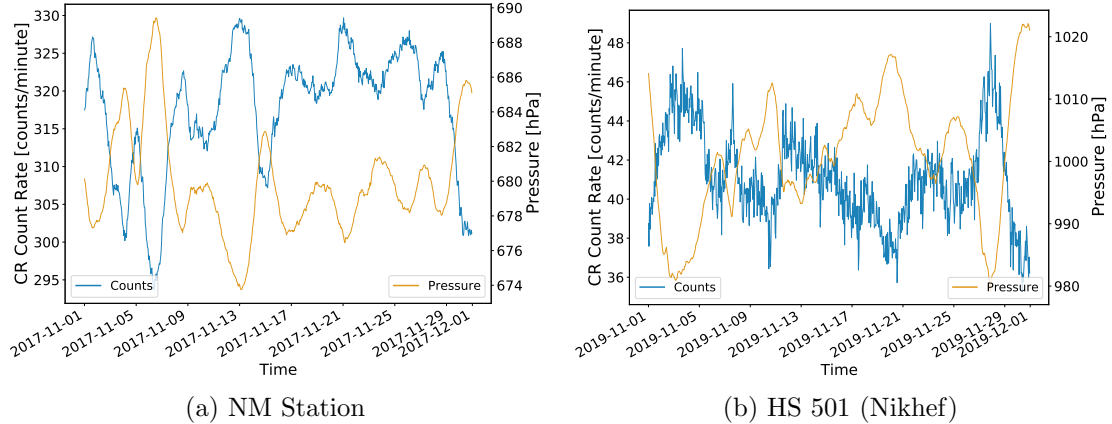


Figure 1.14: ...

The method of correcting for the barometric effect is discussed widely in the literature regarding NMs and is shown to depend on the barometric coefficient. Assuming the cosmic ray flux variation, absent of the atmospheric effects, is reasonably stable, then a simple corrected can be made. The CR variations ( $N$ ) that depend on the local atmospheric pressure are described by equation (1.2), where  $\Delta N$  is the change in count rate,  $\beta$  is the barometric coefficient, and  $\Delta P = P - P_0$  is the deviation in pressure from the average ( $P_0$ ) in the given time-period (Paschalis et al., 2013):

$$\Delta N = -\beta N \Delta P \quad (1.2)$$

Through the integration of equation (1.2), the solution shows the dependence of cosmic ray intensity on pressure as given in equation (1.3).

$$N = N_0 e^{-\beta \Delta P} \quad (1.3)$$

Therefore by taking the logarithm of equation (1.3), one can obtain the barometric coefficient by fitting the straight line given by equation (1.4) to the observed data, where  $N_0$  may be assumed as the mean count rate over the given time-period of observations considered.

$$\ln \left( \frac{N}{N_0} \right) = -\beta \Delta P \quad (1.4)$$

A demonstration of the barometric correction method of fitting a straight line to the data described by equation (1.4) is shown for both a NM and a HiSPARC station in Figure 1.15.

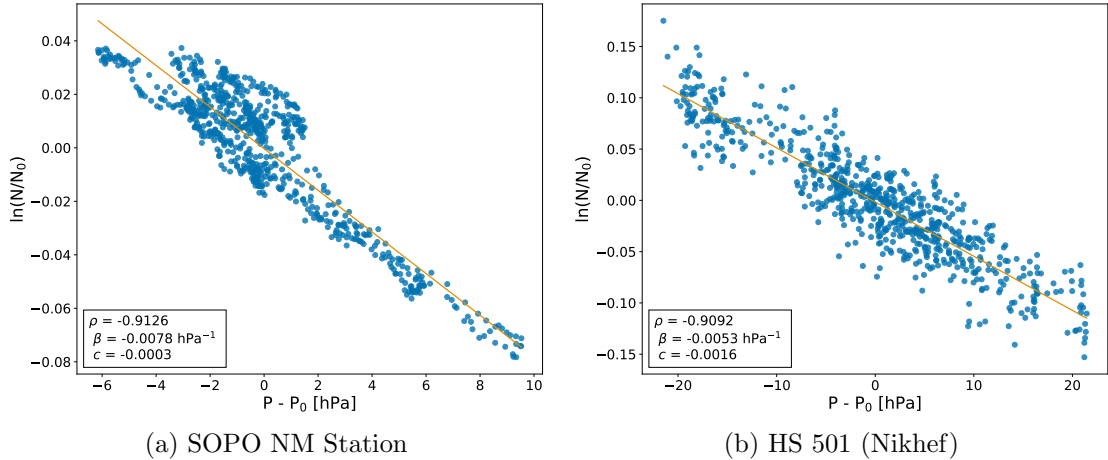


Figure 1.15: The barometric coefficient calculation: (a) during November 2017 for the South Pole (SOPO) NM station, (b) during November 2019 for HiSPARC station 501 at Nikhef.

An online barometric coefficient tool is available which allows user to perform the barometric correction for a given station over a user-defined epoch (<http://cosray.phys.uoa.gr/index.php/data/nm-barometric-coefficient>). Using this tool, it was possible to provide a comparison between the method used in this work to that

of the online NM barometric correction tool which is used for the correction of the NMDB stations. This is provided in Figure 1.16 for monthly corrections throughout 2017 for the NM station at the South Pole (SOPO).

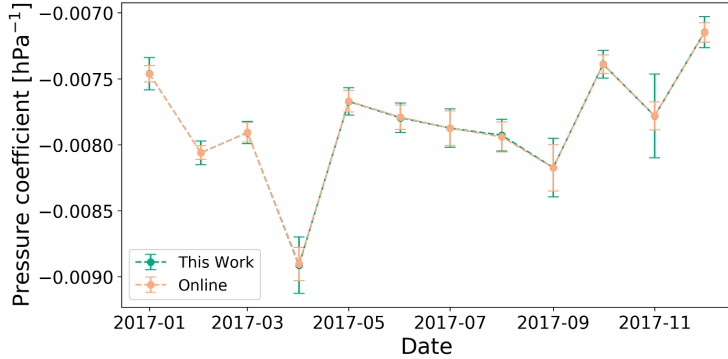


Figure 1.16: A comparison between the monthly barometric coefficient computed in this work and using the online barometric coefficient tool throughout the year 2017 for the SOPO NM station.

Figure 1.16 shows a close agreement between the barometric coefficient calculated in this work and those acquired from the online tool for the SOPO NM. This was also true for other stations tested (APTY and ROME), thus providing confidence that the method used in this work was suitable for application on the HiSPARC data. The barometric correction was performed on the stations where sufficient pressure data and count rates exist, and were re-investigated to determine whether the space weather events were observed in the HiSPARC data. These results are provided in Section 1.7.

### 1.6.3 Temperature Correction

It has been discussed in the literature that the effect of atmospheric temperature on muon intensity has to be treated differently to the pressure effect (Berkova et al., 2011), as the temperature influences both the creation and disintegration processes for muons, such that there is a positive effect and a negative effect on muon intensity as a consequence of temperature variations (Mendonça et al., 2016).

The positive effect is related to pion decay and its dependence on temperature variation. The higher the temperature, the lower the atmospheric pion absorption,

which implies a higher generation rate of muons (Mendon{\c{c}}a et al., 2016).

The negative effect corresponds to the decrease of muon intensity at ground level as the muon average path length varies with temperature. Due to the heating and the expansion of the atmosphere during summer periods muons are produced higher in the atmosphere; hence the muon propagation path increases meaning more atmosphere for muons to traverse before reaching the ground, and an increased decay probability and ionisation losses (Savi et al., 2015; Mendon{\c{c}}a et al., 2016).

Due to the difference in decay probability, the negative effects dominate for low energy muons (i.e. those detected by ground-level MDs), and the positive effect dominates for high energy muons (i.e. those detected by underground MDs) (Berkova et al., 2011); therefore it is expected that the negative effect should dominate for the HiSPARC network. Temperature effects are also observed by NMs; however the effect is less significant than for MDs hence temperature corrections are not widely applied for NMs (Mendon{\c{c}}a et al., 2016).

This is in contradiction with the observations of diurnal variation with the HiSPARC detector, as one can quite clearly see that the HiSPARC stations register higher count rates during local noon.

Several methods of correcting for the negative temperature effect are summarised by Berkova et al. (2011) which utilise different measures of atmospheric temperature when performing the temperature correction. Mendon{\c{c}}a et al. (2016) provides a comparative summary of these methods applied to correct for atmospheric temperature variations observed by GMDN detectors. The methods discussed here however are typically applied over long timescales of years with low temporal resolution rather than to account for short timescale variations with periods of less than a day; hence the suitability of these methods is uncertain.

Mendon{\c{c}}a et al. (2016) concludes that correcting for temperature using the atmospheric mass weighted temperature is one of the most suitable methods for the GMDN as it allows for the highest correlation between long-term CR variations

and temperature. The mass weighted method is an approximation for integrating over the vertical atmospheric temperature as is given in Eq. (1.5):

$$\left(\frac{\Delta N}{N}\right)_T = \bar{\alpha} \int_0^{h_0} \delta T(h) dh = \sum_{i=0}^n \frac{x(h_i) - x(h_{i+1})}{x(h_0)} T(h_i) = \alpha_{\text{MSS}} \delta T_{\text{MSS}} \quad (1.5)$$

where  $h_0$  is the closest to ground altitude;  $\delta T_{\text{MSS}}$  is the deviation of the mass weighted atmospheric temperature;  $T(h_i)$  is the temperature in degrees kelvin observed at the altitude  $h_i$ ;  $x(h_i)$  is the atmospheric depth at the altitude  $h_i$  which is given by Eq. 1.6:

$$x(h) = \int_h^\infty \rho(h) dh \rho(h) = \frac{P(h)}{T(h)} \frac{M_{\text{mol}}}{R} \quad (1.6)$$

where  $P(h)$  is the atmospheric pressure profile as a function of depth;  $T(h)$  is the atmospheric temperature;  $\rho(h)$  is the air density at a given altitude  $h$ ;  $M_{\text{mol}}$  is the molar mass of air;  $R$  is the universal gas constant.

The temperature correction is therefore used in a formalism the same as Eq. (1.4), replacing replacing  $\beta$  for  $\alpha$  and  $\Delta P$  for  $\Delta T$ .

In addition it is discussed by Berkova et al. (2011) and Mendon{\c{c}}a et al. (2016) that the effective generation level temperature is a suitable assumption for this purpose. This method is based on the assumption that muons are mostly generated at a certain isobaric level, taken as 100 mbar, and therefore the temperature at 100 mbar in the atmospheric pressure profile is used,  $T_{100 \text{ mbar}}$ .

As discussed above, Mendon{\c{c}}a et al. (2016) provide this as a method for correcting for the long-term variation in atmospheric temperature which varies seasonally rather than to correct for diurnal variations; therefore it is unsure how relevant this method of atmospheric temperature correction will be to the diurnal variations observed in the HiSPARC data.

## 1.7 HiSPARC Observations After Pressure Corrections

### 1.7.1 Pressure Corrected Observations of Ground Level Enhancements

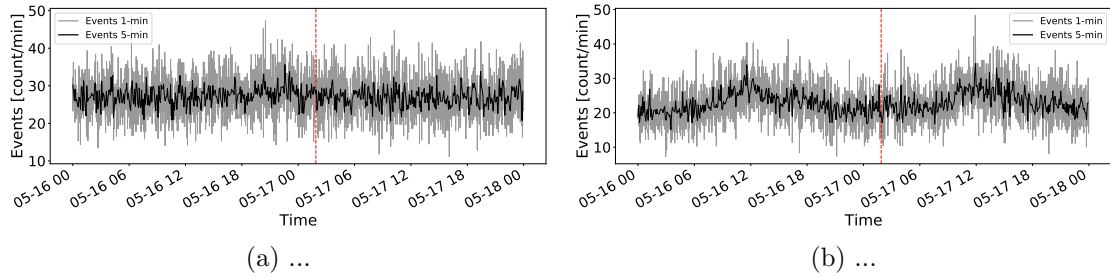


Figure 1.17: Pressure corrected HiSPARC data for 2 stations around the epoch of GLE 71. The top panel of each subplot shows the minute-averaged trigger events between detectors within the station, while the bottom panel shows the mean-shifted, minute-averaged counts by each individual detector in the station. The vertical red, dashed line depicts the approximate onset time of the GLE.

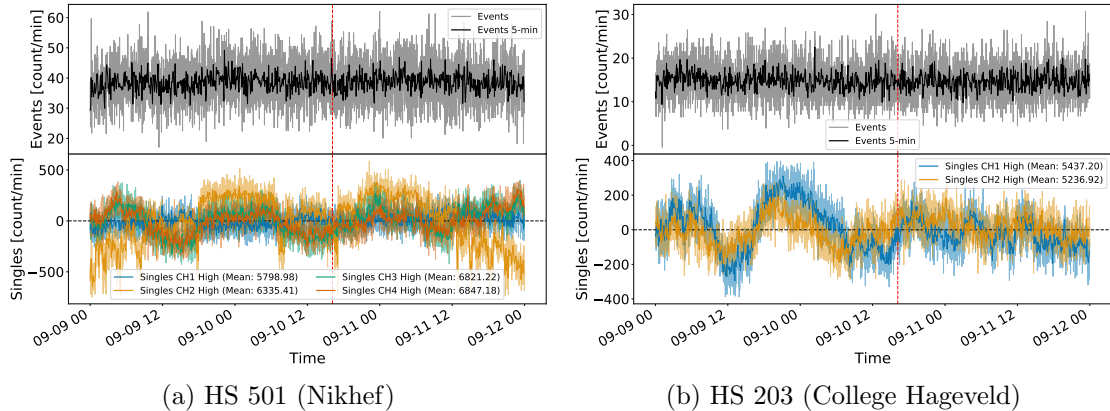


Figure 1.18: Pressure corrected HiSPARC data for 2 stations around the epoch of GLE 72. The top panel of each subplot shows the minute-averaged trigger events between detectors within the station, while the bottom panel shows the mean-shifted, minute-averaged counts by each individual detector in the station. The vertical red, dashed line depicts the approximate onset time of the GLE.

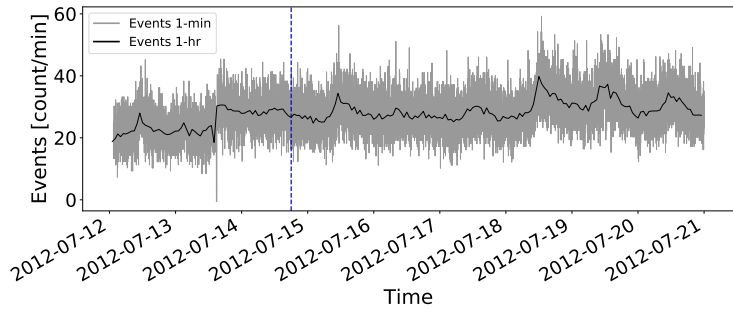


Figure 1.19: ...

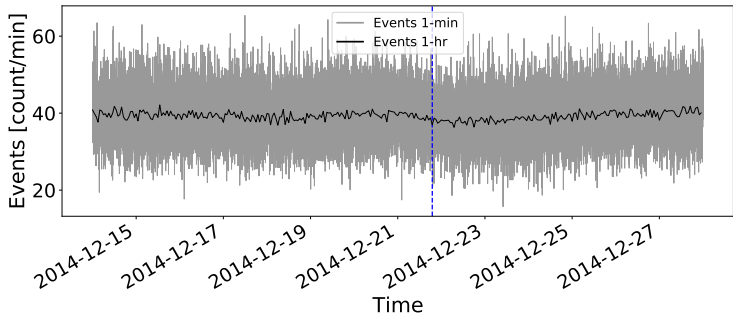


Figure 1.20: ...

### 1.7.2 Pressure Corrected Observations of Forbush Decreases

## 1.8 Discussion

Throughout this chapter the feasibility of using the HiSPARC network of muon detectors has been analysed. This has involved performing cosmic ray air shower simulations using CORSIKA and performing backwards

## 1.9 Conclusion

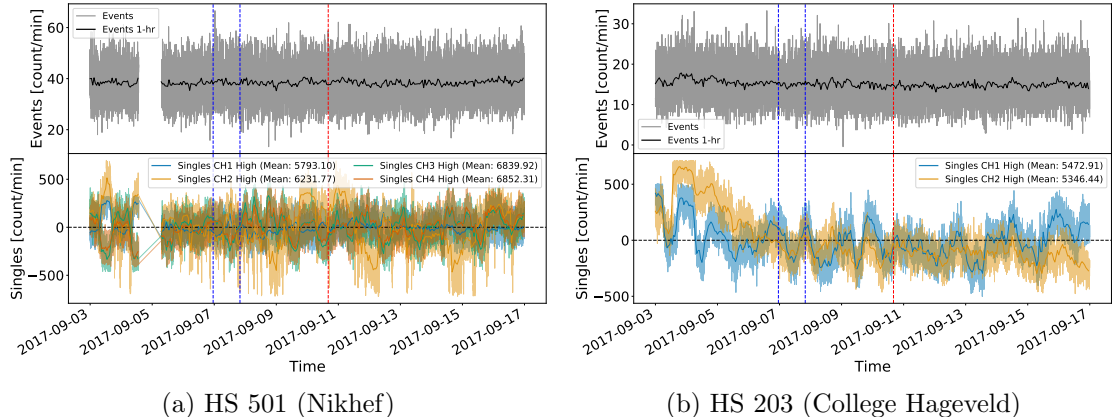


Figure 1.21: Pressure corrected HiSPARC data for [n] stations around the epoch in which there were several FDs close to the onset of GLE 72. The top panel of each subplot shows the minute-averaged trigger events between detectors within the station, while the bottom panel shows the mean-shifted, minute-averaged counts by each individual detector in the station. The vertical blue-dashed lines show the approximate onset-times of the two FDs observed around this epoch and the red-dashed line depicts the approximate onset time of the GLE.

## 2 HiSPARC Station 14008

### 2.1 Introduction

It was clear from the work covered in Chapter 1, using data from the HiSPARC network, that the HiSPARC detectors were not clearly capable of observing space weather events and this is also hindered as they are rather sensitive to variations in the terrestrial conditions.

To some extent, it was possible to eliminate the variation in CRs due to terrestrial variation from the HiSPARC data; however it was shown to be not always so simple, as different detectors in the HiSPARC network showed different responses to pressure and temperature variation. The non-linear relationship between temperature and CR count means the correction of the count rate due to thermal fluctuations is non-trivial, unlike the counterpart correction for pressure.

It is believed that the atmospheric thermal fluctuations induce thermal noise in the Photo Multiplier Tubes (PMTs), and although the temperature inside the HiSPARC ski-boxes have not been measured, it is suspected that the PMTs can get quite hot, in particular when the sky boxes are in direct sunlight.

An instance of thermal noise in a single PMT will be random, and uncorrelated with an instance of thermal noise in another PMT. It is therefore possible to hypothesise that it is unlikely that within the coincidence window of  $\sim 1.5 \mu\text{s}$ , that a coincidence between 2 PMTs would be due to random thermal noise induced in the PMTs.

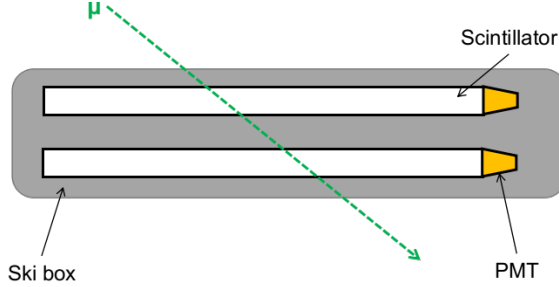


Figure 2.1: Schematic diagram of the HiSPARC station 14008 detector set-up.

To exploit this, it is possible to stack 2 detectors on top of each other to measure a single muon which traverses both scintillators, hence inducing signals in both PMTs.

## 2.2 Aims

The aim of creating a new HiSPARC station was to test whether an alternative configuration of HiSPARC station could minimise atmospheric deviations in the data and allow for the observation of space weather events...

## 2.3 HiSPARC 14008 Detector Set-up

### 2.3.1 Configuration

The configuration of HiSPARC station 14008 is shown in Figure 2.1; the station is composed of two scintillators stacked on top of each other, inside one ski-box.

Each of the plastic scintillators has a thickness of  $\Delta x = 0.5$  cm, and density,  $\rho = TBC \text{ gcm}^{-3}$ . We know that the stopping power of the scintillator for a minimum ionising particle is  $\sim 2 \text{ MeV/cm}^{-2}$  [REF]... [discuss this w/ Angela as it seems to be derivative of Blethe-Bloch, but cannot find link]...

$$E = \Delta x S \rho \cos(\theta) \quad (2.1)$$

Bartels (2012) state that typical energy loss of a muon in a single scintillator is 3.38 MeV, hence in this configuration, as a muon traverses two scintillators, the

lower limit on the energy loss by muons in the detector is  $\sim 6.76$  MeV.

To protect the scintillators and PMTs within the ski boxes, we sandwiched the scintillators between layers of foam, as can be seen on the lab work bench in Figure 2.2a. Upon complete assembly of the detector, the scintillators and PMTs are placed within the ski-box on the roof of the Poynting Physics building on the campus of the University of Birmingham, as shown in Figure 2.2b.

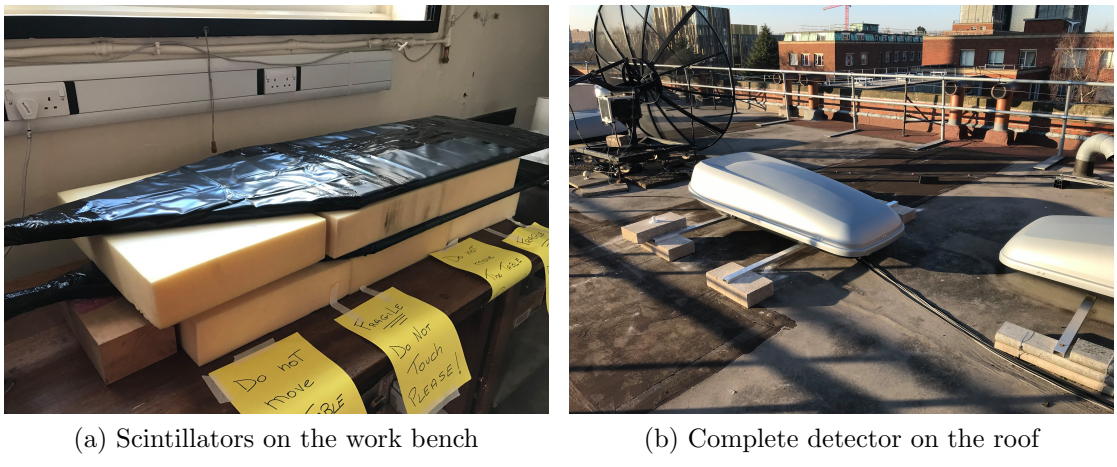


Figure 2.2: HiSPARC 14008 assembly and configuration. (a) shows the stacked arrangement of the scintillators on the lab work bench, between layers of protective foam. (b) shows the complete detector inside the ski-box on the University of Birmingham campus.

### 2.3.2 Calibration

When setting up the HiSPARC station, it was required to set several operating parameters for the detectors and the HiSPARC electronics box. One such setting was the PMT operating voltage. Each of the detector PMTs needs to be powered with a high enough operating voltage such to provide an amplified signal, but not too high such as to over-amplify the noise.

In general, the PMTs have an advised operating voltage of around 700 V (Fokkema, 2019); however, best practise is to operate the PMT at the plateau region, whereby the counts/voltage no longer increases. As can be seen from Figure 2.3, neither of the PMTs have clear plateau regions, hence there was no obvious PMT set point.

The HiSPARC installation manual does, however, suggest to tune the PMT

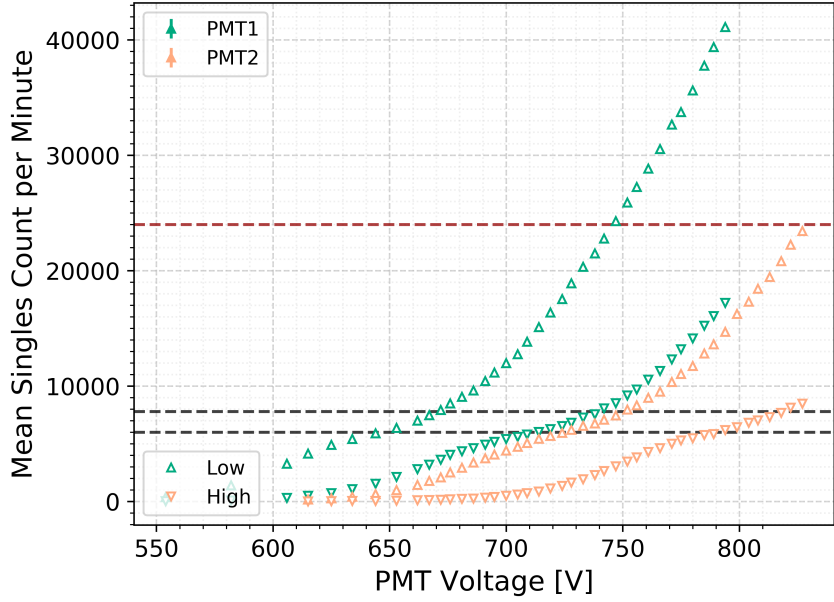


Figure 2.3: Voltage calibration curve for the PMTs of station 14008. The upper, red-dashed line indicates the upper limit for the low threshold singles rate (400 Hz), and the lower 2, black-dashed lines indicate the upper and lower bounds for the high threshold singles rate (100–130 Hz).

voltages such that the singles rates for each detector meet the following criteria: singles rate of 100–130 Hz for signal above the high trigger threshold, and singles rate of <400 Hz for signal above the low trigger threshold (Fokkema, 2019).

In order to calibrate the PMTs to the correct level, we measured the singles rates above the high and low thresholds as a function of PMT operating voltage, as is shown in Figure 2.3 [UPDATE THIS PLOT...!!!!]. The voltage calibration plot shows drastically the different performances one can get from different PMTs, therefore it is necessary to treat each PMT individually when calibrating.

### 2.3.3 Monitoring Temperature

It was suspected in Chapter 1 that the singles count rates (and thus event count rates also) are affected by the temperature of the PMT within the HiSPARC ski-boxes.

Some of the existing HiSPARC stations monitor local temperature however none measure the temperature of the PMT within the ski box; therefore the temperature of the PMT itself is unknown, and thus we cannot account for the thermal noise.

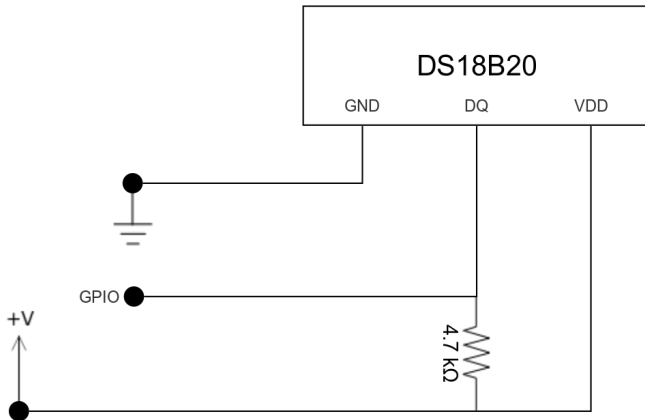


Figure 2.4: Schematic diagram of the DS18B20 temperature sensor circuit, whereby the voltage, ground, and GPIO interfaces connect directly into pins of the Raspberry Pi board.

When building this new HiSPARC station, a temperature sensor was placed into the ski box which allowed us to monitor the temperature.

Figure 2.4 shows the schematic for the temperature sensor. We used the DS18B20 temperature sensor with the one-wire telemetry protocol, which used a single wire to transmit the temperature readings to the microcontroller; the microcontroller used was a Raspberry Pi 4. Three wires were used for the operation of the DS18B20: constant current voltage, ground, and data.

We use the Raspberry Pi to control the data acquisition by running a Python program to output the temperature readings from the sensor to a local file. The temperature is read on a 10-second cadence and is recorded in degrees Celsius.

## 2.4 Observations

## 2.5 Conclusions

# Bibliography

- Bartels R. T., 2012, Technical report, The HiSPARC Experiment: An Analysis of the MPV and the Number of Events per Unit Time. University College Utrecht
- Berkova M. D., Belov A. V., Eroshenko E. A., Yanke V. G., 2011, Bull. Russ. Acad. Sci. Phys., 75, 820
- Desorgher L., Flckiger E. O., Gurtner M., 2006. p. 2361, <http://adsabs.harvard.edu/abs/2006cosp...36.2361D>
- Fokkema D. B. R. A., 2012, PhD thesis, University of Twente
- Fokkema D. B. R. A., 2019, HiSPARC station software en hardware documentatie HiSPARC software 6.11 documentation, <https://docs.hisparc.nl/station-software/doc/index.html>
- Heck D., Pierog T., 2017, Technical Report 7.6400, Extensive Air Shower Simulation with CORSIKA: A Users Guide
- Herbst K., Kopp A., Heber B., 2013, Annales Geophysicae, 31, 1637
- Lingri D., Mavromichalaki H., Belov A., Eroshenko E., Yanke V., Abunin A., Abunina M., 2016, arXiv:1612.08900 [astro-ph]
- Mendonça R. R. S. d., et al., 2016, ApJ, 830, 88
- Paschalis P., Mavromichalaki H., Yanke V., Belov A., Eroshenko E., Gerontidou M., Koutroumpi I., 2013, New Astronomy, 19, 10
- Savi M., Maleti D., Jokovi D., Veselinovi N., Banjanac R., Udovii V., Dragi A., 2015, J. Phys.: Conf. Ser., 632, 012059
- van Dam K., van Eijk B., Fokkema D. B. R. A., van Holten J. W., de Laat A. P. L. S., Schultheiss N. G., Steijger J. J. M., Verkooijen J. C., 2020, Nuclear Instruments and Methods in Physics Research Section A: Accelerators, Spectrometers, Detectors and Associated Equipment, 959, 163577